Optics Letters

Millimeter-wave generation based on a monolithic dual-wavelength DFB laser with four phase-shifted sampled gratings and equivalent chirp technology

Bocheng Yuan,[1,*] Yizhe Fan,[1] Simeng Zhu,[1] Weiqing Cheng,[1] Yunshan Zhang,[2] Xiangfei Chen,[3] Shengwei Ye,[1] Song Liang,[4] Yongguang Huang,[4] Ruikang Zhang,[4] Jehan Akbar,[1] John H. Marsh,[1] and Lianping Hou[1]

[1]James Watt School of Engineering, University of Glasgow, Glasgow G12 8QQ, UK
[2]College of Electronic and Optical Engineering, Nanjing University of Posts and Telecommunications, Nanjing 210046, China
[3]College of Engineering and Applied Sciences, Nanjing University, Nanjing 210093, China
[4]Institute of Semiconductors, Chinese Academic of Sciences, Beijing 100083, China
*2644187y@student.gla.ac.uk

Received 29 August 2023; revised 11 September 2023; accepted 11 September 2023; posted 12 September 2023; published 26 September 2023

A dual-wavelength DFB laser array based on four phase-shifted grating and equivalent chirp technology is first proposed, fabricated, and experimentally demonstrated. The dual-wavelength emitting is achieved by symmetrically introducing two π phase shifts into a chirped four phase-shifted sampled grating cavity. Meanwhile, the beating signal of the dual-wavelength output is stabilized by applying an electro-absorption modulator integrated at the rear of the cavity. Under different grating chirp rates, a series of RF signals from 66.8 GHz to 73.6 GHz with a linewidth of less than 210 kHz is obtained.

https://doi.org/10.1364/OL.504585

Introduction. Photonic generation of millimeter-wave (mm-wave) signals is attractive for numerous applications, such as radio-over-fiber, broadband wireless access networks, radar, and satellite communications, and has been intensively investigated over the past few years [1]. Due to the availability of extremely low-loss and low-cost optical fiber transmission systems, photonics technology is often preferred for generating mm-waves over conventional electronics. Normally, the approach for generating mm-wave signals in the optical domain is to beat two optical signals generated by two separate single longitudinal mode (SLM) lasers in a photodetector (PD). The beating signal has a frequency equal to the frequency difference between the two optical signals, and the beating signal quality is susceptible to external influences such as temperature and vibration, as these factors can affect the two separate lasers differently.

In comparison, utilizing a monolithically dual-wavelength laser (DWL) for beat frequency generation is more appealing. In a DWL, the two optical signals are generated in a single cavity by injecting current through a single electrode on the ridge waveguide. The impact of temperature variations on the frequency difference between the two lasing modes is negligible since the temperature drift affects the two wavelengths identically. Moreover, no external polarization controller is required before the two optical signals are input into the PD because they are generated within the same cavity.

In this paper, for the first time we have proposed and experimentally demonstrated a DWL array based on four phase-shifted sampled gratings (4PS) combined with equivalent grating chirp technology. The core of the equivalent chirp technology lies in modulating sampling periods at the micron scale to achieve complex grating responses in the ±1st channel [2]. In a linearly chirped grating cavity, the peaks in photon distributions of the two lasing modes are separated along the cavity, and mode competition is significantly suppressed [3]. However, the grating coupling coefficient κ of a conventional sampled Bragg grating (C-SBG) in the ±1st channel is only 1/π of that of a uniform Bragg grating (UBG). The 4PS structure can significantly enhance the κ value. Therefore, our new configuration not only enables equivalent chirp modulation through the adjustment of sampling periods but also achieves a κ in the +1st channel reaching 0.9 times that of a UBG while suppressing the zeroth grating reflection [4,5].

An electro-absorber (EA) section is also integrated with the DFB laser to enhance the phase stabilization between the two lasing modes [6]. By setting a series of chirp rates from 30 nm/mm to 90 nm/mm, we obtained radio frequency (RF) signals from 66.8 GHz to 73.6 GHz, with the linewidth ranging from 118 kHz to 210 kHz. It is worth noting that, compared to previously reported DWLs [3,7,8], we have achieved the narrowest linewidth with the shortest cavity length.

Device fabrication and experimental results. The epitaxial structure of the device emitting at 1.55 μm is based on an AlGaAsIn–InP heterostructure as reported in [9], and the fabrication process is the same as described in [6]. A schematic of the fabricated device is shown in Fig. 1(a). The device comprises an EA section (30 μm) and a DFB section (700 μm), separated

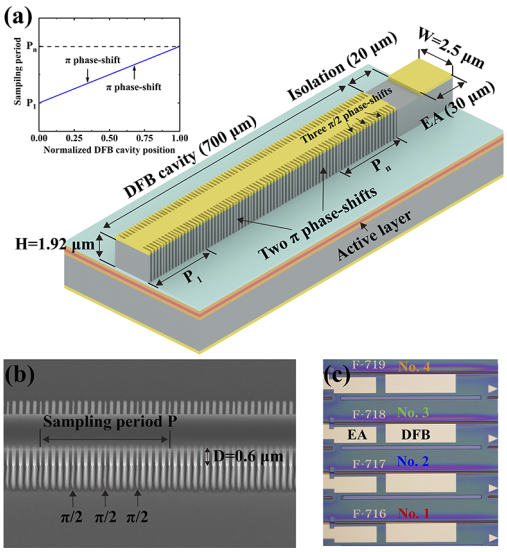

Fig. 1. (a) Schematic of the proposed device, with the inset showing the sampling period distribution along the cavity. (b) Scanning electron microscope image of the etched ridge waveguide and 4PS sidewall grating. (c) Microscope image of the DWL array.

by an electrical isolation groove (20 μm). The ridge waveguide width W is 2.5 μm and the height H is 1.92 μm; the effective refractive index of the guide mode (TE_0) is estimated to be 3.19. Both sidewalls have the same uniform seed grating with a period of 257 nm and a recess depth D of 0.6 μm. As shown in the inset in Fig. 1(a), the sampled periods are linearly modulated along the DFB laser cavity to achieve an equivalent chirp modulation, the chirp rate being defined as the ratio of the difference between the first and last sampling periods (P_n–P_1) to the length of the DFB cavity. Every sample period employs the 4PS structure. Two π phase shifts are introduced at positions 1/3 and 2/3 along the length of the DFB cavity to ensure dual-wavelength lasing. Figure 1(b) is a scanning electron microscope image of the etched ridge waveguide and 4PS sidewall grating. In the 4PS structure, the grating in each sampling period is evenly divided into four sections, with each adjacent grating section subjected to a π/2 phase shift. Compared to a C-SBG in which half of the sampling period has no grating, the 4PS structure retains a high grating coupling coefficient in the +1st-order channel, while suppressing the zeroth-order reflection [5]. Figure 1(c) is a microscope image of the fabricated four DWL arrays. The four devices (No.1 to No.4) have the same structure but different chirp rates of 30 nm/mm, 50 nm/mm, 70 nm/mm, and 90 nm/mm, respectively. After fabrication, the laser chip was cleaved into bars, with both facets left uncoated.

The simulation results in Figs. 2(a) and 2(b) illustrate the impact of grating chirp on the photon distribution of the two lasing modes. As shown in Fig. 2(a), in the absence of the grating chirp, the photon distribution peaks of the two lasing modes nearly coincide, concentrating at the positions of two π phase shifts. In comparison, when the equivalent chirp is applied, the peaks of photon distributions are separated, and the overlap region significantly decreases, thereby reducing a competition between the two lasing modes within the cavity. Figure 2(c) shows the simulated spectrum obtained using the traveling-wave method [10]. The two lasing modes (λ_1 and λ_2) are clearly observed, and two four-wave mixing signals (FWM

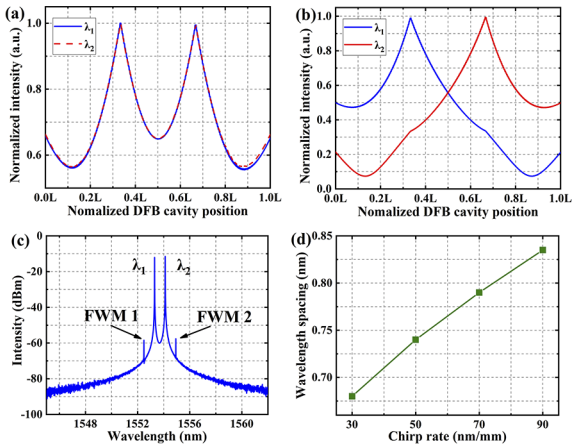

Fig. 2. (a) Calculated photon distribution without a chirp. (b) Calculated photon distribution with a chirp. (c) Simulated optical spectrum. (d) Calculated wavelength spacing versus the chirp rate.

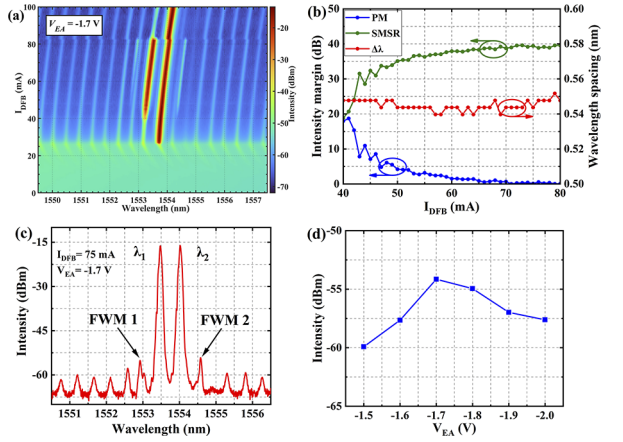

Fig. 3. (a) 2D optical spectrum map of a laser with 30 nm/mm chirp rate when $V_{EA} = -1.7$ V. (b) PM, SMSR, and Δ_λ versus I_{DFB}. (c) Measured optical spectrum of the laser when $I_{DFB} = 75$ mA, $V_{EA} = -1.7$ V. (d) Maximum FWM signal intensity as a function of V_{EA} with $I_{DFB} = 75$ mA.

1 and FWM 2) appear on either side of them. The four-wave mixing signals result from fluctuations induced in the carrier density (and hence variations in the gain) caused by the beating of λ_1 and λ_2 [10]. Figure 2(d) illustrates the relationship between the wavelength spacing and the chirp rate. As the chirp rate increases, the wavelength spacing becomes larger; therefore, different chirp rates were designed to generate different RF frequencies.

Testing of the devices was carried out under continuous-wave (CW) conditions, with the laser array mounted on a copper heat sink at 20 °C. The optical outputs were measured from the DFB facet using an optical spectrum analyzer (OSA) with a 0.06 nm resolution bandwidth (RBW). Figure 3(a) depicts the operational characteristics of the device with a chirp rate of 30 nm/mm, with an EA biased at –1.7 V ($V_{EA} = -1.7$ V). It can be observed that the device exhibits a favorable dual-mode operation state when the DFB injection current (I_{DFB}) is within the range of 45–81 mA, and due to the presence of facet reflections, the device experiences mode hopping at 82 mA [11]. Figure 3(b) shows the power margin between λ_1 and λ_2 (PM), sidemode suppression

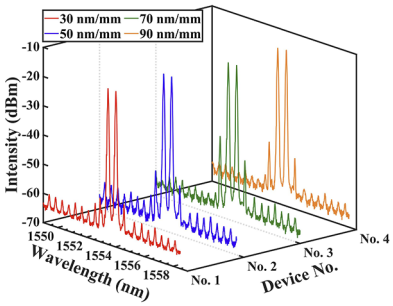

Fig. 4. Measured optical spectrum of the DWLs with different chirp rates.

Table 1. Parameters of the Array

Device No.	Chirp Rate	I_{DFB}	V_{EA}	$\Delta\lambda$
No. 1	30 nm/mm	75 mA	−1.7 V	0.539 nm
No. 2	50 nm/mm	98 mA	−1.2 V	0.549 nm
No. 3	70 nm/mm	128 mA	−0.6 V	0.575 nm
No. 4	90 nm/mm	145 mA	−1.9 V	0.595 nm

ratio (SMSR), and wavelength spacing ($\Delta\lambda$) under different I_{DFB}. When I_{DFB} exceeds 55 mA, the PM remains within 3 dB, and it is less than 0.5 dB when I_{DFB} is between 70 mA and 80 mA; a lower PM is beneficial for improving the quality of the beating signal. When I_{DFB} is higher than 45 mA, the SMSR consistently remains above 30 dB. The wavelength separation, $\Delta\lambda$, falls in the range 0.539 nm to 0.551 nm, with a variation of 0.012 nm. Considering that this variation is smaller than the RBW of the OSA, the $\Delta\lambda$ is independent of the injection current, implying that the beat signal's center frequency is relatively stable. Figure 3(c) displays the measured spectrum when $V_{EA} = -1.7$ V and $I_{DFB} = 75$ mA. The results are consistent with the simulation, clearly showing the presence of two lasing modes and two FWM signals. It should be noted that significant Fabry–Perot (FP) modes are also observed in the spectrum due to the presence of facet reflections. Figure 3(d) shows the intensity variation of the larger FWM signal under a different V_{EA}. The FWM intensity reaches its maximum when $V_{EA} = -1.7$ V. For the proposed device, a stable dual-mode output can be achieved by adjusting the V_{EA} within a certain range [6]. In the subsequent experiments, the device data were obtained at the optimal V_{EA} where the FWM signal was the strongest.

The measured spectra and operating parameters of the array are shown in Fig. 4 and Table 1, respectively. Figure 4 shows typical spectra of the four devices with different chirp rates, each demonstrating good dual-mode characteristics with clear visibility of the FWM signals. Meanwhile, due to the facet reflection caused by cleaving, each device exhibits FP modes in the spectrum. However, these FP modes have a minimal impact on the beat frequency signal as the power ratio between the main modes and the FP modes is higher than 45 dB.

According to Table 1, a larger chirp rate results in a larger wavelength difference, which is consistent with the simulation results shown in Fig. 2(d). Additionally, it can be observed that devices with larger chirp rates require higher injection currents to achieve stable dual-wavelength lasing. This phenomenon can be attributed to an increase in the chirp rate leading to an increase in the threshold gain margin between λ_1 and λ_2. As a result, the device requires a higher injection to compensate for the weaker mode, thereby achieving equal output power for λ_1 and λ_2 [3].

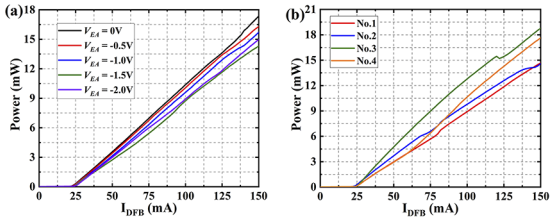

Fig. 5. (a) Measured P–I curves of the device with 30 nm/mm chirp rate under a different V_{EA}, (b) P–I curves of the devices with the different chirp rate for values of V_{EA} shown in Table 1.

Figure 5(a) shows typical power-injection current (P–I) characteristics from the DFB output side under a different V_{EA} with a scan step of 2 mA. The threshold current and output facet slope efficiency with 0 V applied to the EA section were 24 mA and 13.8% W/A, respectively. When the EA reverse voltage was increased from 0 V to −1.5 V, the threshold current was unchanged, but the slope efficiency was reduced as a result of an increase in an interband and exciton absorption. With further increase of the reverse voltage to −2.0 V, the DFB laser became optically isolated from the facet reflection and the slope efficiency increased, with the threshold current still unchanged. This indicates that the DFB laser was working as an independent cavity and the partitioning electrical slot prevented electrical coupling between the DFB and EA sections. Figure 5(b) shows the P–I curves of the four devices under the V_{EA} values shown in Table 1. Within the limit of 2 mA scanning steps, the threshold currents of the different devices are the same at 24 mA.

However, the four devices exhibit different slope efficiencies which can be attributed to the fact that the devices operate at different V_{EA}, and the different grating coupling coefficients resulting from different chirp rates also affect the efficiency [12]. It can be seen that there are some kinks in the P–I curves, which are indicative of mode hopping phenomena. For example, in the P–I curve of device No. 1 (red line in Fig. 5(b)), a kink is observed at 82 mA, corresponding to the mode hop seen in Fig. 3(a).

The RF signal was measured using a PD (u^2t Photonics XPDV2020R 50 GHz) connected to an electrical spectrum analyzer (ESA). The optical signal was coupled by a lensed fiber from the device and then directly input into the PD without external phase adjustment or polarization control. A mixer (Keysight 11970V) is also utilized in the system to extend the measurement range of the ESA. Figure 6(a) shows the RF signals of the array measured under the conditions shown in Table 1; the ESA was set with an RBW of 100 kHz and a scanning range of 15 GHz. Consistent with the simulation results, the device with a higher chirp rate has an RF signal at a higher frequency. The variation of the RF linewidth with I_{DFB} is shown in Fig. 6(b). Since the RF signal is generated by beating λ_1 and λ_2, the linewidth of the signal is primarily influenced by three factors. One factor is the PM between λ_1 and λ_2, and when the PM is too large, the beat signal will become poor or even undetectable. The second factor is that the linewidth of the optical signal tends to decrease as the injection current increases [13]. The third factor is the facet reflection from the DFB side (up to 30%) can induce self-injection effects in the device, also leading to a reduction in linewidth [14]. Figure 6(c) shows the fitted linewidth of the device with 70 nm/mm chirp rate under $V_{EA} = -0.6$ V, $I_{DFB} = 128$ mA. During the linewidth measurement, the ESA was

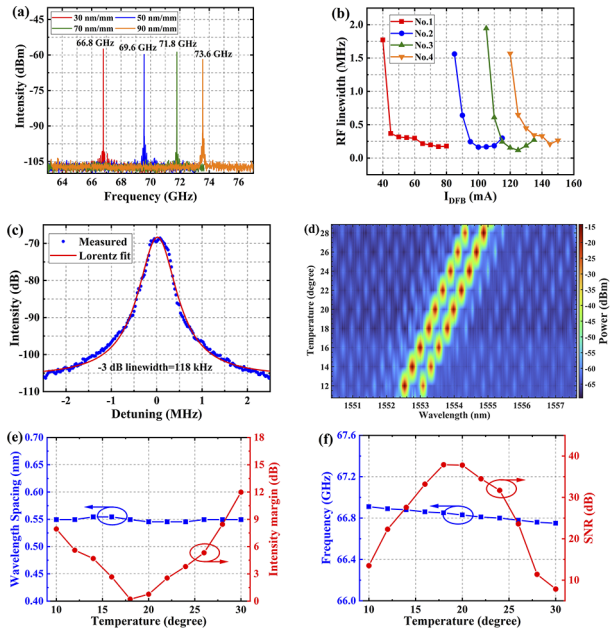

Fig. 6. (a) Measured RF signals of the DWL array. (b) RF signal linewidth of the array versus I_{DFB}. (c) Fitted linewidth curve of the device with a 70 nm/mm chirp rate. (d) 2D optical spectrum. (e) Wavelength spacing and PM. (f) RF frequency and SNR versus TEC temperature of the device with 70 nm/mm chirp rate under $I_{DFB} = 75$ mA and $V_{EA} = -1.7$ V.

set with an RBW of 51 kHz and a scanning range of 80 MHz, and the –3 dB linewidth was obtained by measuring the –20 dB bandwidth and dividing by $\sqrt{99}$ to reduce the measurement error [15]. The performance of the device was also assessed as a function of the heat sink temperature over the range from 10 °C to 30 °C in steps of 2 °C. From Figs. 6(d) and 6(e), it is evident that within this temperature range, the device maintains a dual-wavelength operation. It is important to note that, despite the increase in the effective refractive index of the waveguide due to the rising temperature causing both modes to experience a redshift, the $\Delta\lambda$ remains constant. This is because the two lasing wavelengths are generated within the same DFB cavity, and the rate of temperature-induced wavelength shift is the same for both wavelengths. The increase in temperature leads to a redshift in the gain peak, causing an imbalance in gain between the two modes and an increase in PM. In Fig. 6(f), the RF frequency decreases slightly with increasing temperature due to the overall redshift of the two lasing wavelengths [7]. The deterioration in the RF signal-to-noise ratio (SNR) is caused by the increased PM. The RF signal frequencies and lowest measured linewidths of the array at 20 °C are shown in Table 2. Table 3 presents a comprehensive comparison between the devices described in this paper and previously reported DWLs [3,7,8]. It is evident that the devices introduced in this paper (referred to as type 1) achieve the narrowest RF signal linewidth, spanning from 118 kHz to 210 kHz, while also exhibiting this outstanding performance with the shortest cavity length of 750 µm.

Conclusion. This paper presents a dual-wavelength laser array based on a 4PS grating and equivalent chirp technology. The 4PS structure enables a chirped grating to be implemented by modulating the sampling period at the micron scale while maintaining a relatively high grating coupling coefficient. The introduction of the chirp reduces mode competition, enabling the device to produce two stable longitudinal modes. By designing different chirp rates, different wavelength spacings are achieved. The RF signals range from 66.8 GHz to 73.6 GHz with linewidths from 118 kHz to 210 kHz. Experimental results demonstrate that this device has the potential to be a highly integrated and easy-to-operate source of mm-waves.

Table 2. RF Signal Frequency and Linewidth

Device No.	I_{DFB}	V_{EA}	Frequency	Linewidth
No. 1	75 mA	−1.7 V	66.8 GHz	170 kHz
No. 2	98 mA	−1.2 V	69.6 GHz	164 kHz
No. 3	128 mA	−0.6 V	71.8 GHz	118 kHz
No. 4	145 mA	−1.9 V	73.6 GHz	210 kHz

Table 3. Comparison with Previous DWLs

Type	Cavity Length	Frequency	Linewidth
1	750 µm	66.8–73.6 GHz	118–210 kHz
2	1000 µm	88.5 GHz	5.1 MHz
3	1000–1200 µm	50–59 GHz	250–850 kHz
4	1200 µm	64 GHz	800 kHz

Funding. Engineering and Physical Sciences Research Council (EP/R042578/1).

Acknowledgment. We would like to acknowledge the staff of the James Watt Nanofabrication Centre at the University of Glasgow for their help in fabricating the devices, and Dr. Jue Wang for the assistance in setting up the RF signal measure platform.

Disclosures. The authors declare no conflict of interest.

Data availability. Data underlying the results presented in this paper are not publicly available at this time but may be obtained from the authors upon reasonable request.

REFERENCES

1. D. Marpaung, J. Yao, and J. Capmany, Nat. Photonics **13**, 80 (2019).
2. Y. Dai and J. Yao, IEEE J. Quantum Electron. **44**, 938 (2008).
3. Y. Zhang, B. Yuan, J. Shi, W. Qi, L. Li, L. Wang, J. Zheng, S. Guan, T. Fang, and X. Chen, IEEE J. Quantum Electron. **58**, 1 (2022).
4. Y. Dai, X. Chen, L. Xia, Y. Zhang, and S. Xie, Opt. Lett. **29**, 1333 (2004).
5. J. Li, Y. Cheng, Z. Yin, L. Jia, X. Chen, S. Liu, S. Li, and Y. Lu, IEEE Photonics Technol. Lett. **21**, 1639 (2009).
6. L. Hou, M. Haji, I. Eddie, H. Zhu, and J. H. Marsh, Opt. Lett. **40**, 182 (2015).
7. B. Yuan, Y. Fan, S. Ye, Y. Zhang, Y. Sun, X. Sun, W. Cheng, S. Liang, Y. Huang, R. Zhang, J. Wang, J. Marsh, and L. Hou, J. Lightwave Technol. **41**, 1 (2023).
8. S. Li, R. Li, L. Li, R. Liu, L. Gao, and X. Chen, IEEE Photonics Technol. Lett. **25**, 299 (2013).
9. L. Hou, P. Stolarz, J. Javaloyes, R. P. Green, C. N. Ironside, M. Sorel, and A. C. Bryce, IEEE Photonics Technol. Lett. **21**, 1731 (2009).
10. J. E. Carroll, J. Whiteaway, and D. Plumb, *Distributed Feedback Semiconductor Lasers* (IET, 1998), Vol. 10.
11. O. Nilsson and J. Buus, IEEE J. Quantum Electron. **26**, 2039 (1990).
12. S. K. C. Liew, IEEE Photonics Technol. Lett. **7**, 1400 (1995).
13. J. Liu, X. Zhan, H. Yan, and W. Yang, in *2017 4th International Conference on Industrial Economics System and Industrial Security Engineering (IEIS)* (IEEE, 2017), pp. 1–6.
14. H. G. Zhang, N. H. Zhu, J. W. Man, J. H. Ke, B. H. Zhang, W. Han, W. Chen, H. Q. Yuan, X. Wang, L. Xie, L. J. Zhao, and W. Wang, IEEE Photonics Technol. Lett. **21**, 1045 (2009).
15. Z. Zhao, Z. Bai, D. Jin, Y. Qi, J. Ding, B. Yan, Y. Wang, Z. Lu, and R. P. Mildren, Opt. Express **30**, 30600 (2022).